International Journal of Heat and Fluid Flow 45 (2014) 41–52

Contents lists available at ScienceDirect

International Journal of Heat and Fluid Flow

journal homepage: www.elsevier.com/locate/ijhff

Measurement of local heat transfer coefficient during gas–liquid Taylor bubble train flow by infra-red thermography

Balkrishna Mehta, Sameer Khandekar *

Department of Mechanical Engineering, Indian Institute of Technology Kanpur, Kanpur, UP 208016, India

ARTICLE INFO

Article history:
Received 12 January 2013
Received in revised form 6 October 2013
Accepted 2 December 2013
Available online 25 December 2013

Keywords:
Taylor bubble flow
Local Nusselt number
InfraRed Thermography
Design of experiment
Heat transfer enhancement

ABSTRACT

In mini/micro confined internal flow systems, Taylor bubble train flow takes place within specific range of respective volume flow ratios, wherein the liquid slugs get separated by elongated Taylor bubbles, resulting in an intermittent flow situation. This unique flow characteristic requires understanding of transport phenomena on global, as well as on local spatio-temporal scales. In this context, an experimental design methodology and its validation are presented in this work, with an aim of measuring the local heat transfer coefficient by employing high-resolution InfraRed Thermography. The effect of conjugate heat transfer on the true estimate of local transport coefficients, and subsequent data reduction technique, is discerned. Local heat transfer coefficient for (i) hydrodynamically fully developed and thermally developing single-phase flow in three-side heated channel and, (ii) non-boiling, air–water Taylor bubble train flow is measured and compared in a mini-channel of square cross-section (5 mm × 5 mm; D_h = 5 mm, $Bo \approx 3.4$) machined on a stainless steel substrate (300 mm × 25 mm × 11 mm). The design of the setup ensures near uniform heat flux condition at the solid–fluid interface; the conjugate effects arising from the axial back conduction in the substrate are thus minimized. For benchmarking, the data from single-phase flow is also compared with three-dimensional computational simulations. Depending on the employed volume flow ratio, it is concluded that enhancement of nearly 1.2–2.0 times in time-averaged local streamwise Nusselt number can be obtained by Taylor bubble train flow, as compared to fully developed single-phase flow. This enhancement is attributed to the intermittent intrusion of Taylor bubbles in the liquid flow which drastically changes the local fluid temperature profiles. It is important to maintain proper boundary conditions during the experiment while estimating local heat transfer coefficient, especially in mini-micro systems.

1. Introduction

Transport mechanisms of heat, momentum and species under two-phase flow conditions in mini/micro systems are greatly affected by local distribution of the phases or flow patterns in the channel. Taylor bubble train flow, a sub-set of slug flows occurring in mini/micro-systems, is typically characterized by a sequence of long bubbles which are trapped in between liquid slugs. Geometrical distribution of the liquid slugs and bubbles is fundamentally governed by the resultant of gravity, surface tension, inertia and viscous effects. For a given liquid–gas system, interplay between the gravity and surface tension forces mainly depends on the size of the channel, i.e. the applicable Bond number (*Bo*). When surface tension dominates over gravitational body force, Taylor bubbles adopt the characteristic capsular shape, with a liquid thin film separating the gas/vapor phase with the wall. In horizontal flow conditions when *Bo* is high enough ($Bo > Bo_{cr} \approx 1.835$ (Bretherton, 1961)), gravity force dominates over surface tension and the liquid film essentially takes the lower part of the channel cross-section, whereas in the upper part, a negligibly thin liquid film may or may not exist. The existence of liquid film on the wall depends on *Ca* and surface energy characteristics (hydrophobic or hydrophilic) of the channel wall (Serizawa et al., 2002; Cubaud and Ho, 2004; Ajaev and Homsy, 2006).

Taylor bubble train flow is expected to occur and, is employed in many new and upcoming systems and devices in diverse branches of engineering ranging from bio-medical, bio-chemical to thermal management of electronics, micro-two-phase heat exchangers and reactors, nuclear rod bundles, micro-fluidic devices, loop heat pipes, etc. (Triplett et al., 1999; Devesenathipathy et al., 2003; Spernjak et al., 2007; Moharana et al., 2011a). Quite frequently, due to the mini/micro fabrication techniques, such as laser machining, chemical etching, micro-milling, abrasive jet machining etc., emerging technological solutions employing internal convective flows, make use of channels of non-circular cross sections. Rectangular micro-channels are of particular interest as they are used extensively in heat sinks of microelectronic devices,

* Corresponding author. Tel.: +91 512 259 7038; fax: +91 512 259 7408.
E-mail address: samkhan@iitk.ac.in (S. Khandekar).

0142-727X/$ - see front matter © 2013 Elsevier Inc. All rights reserved.
http://dx.doi.org/10.1016/j.ijheatfluidflow.2013.12.001

Nomenclature

A	area of cross section (m^2)
c_p	specific heat at constant pressure (J/kg K)
D_h	hydraulic diameter (m)
Δf	number of frames
h	heat transfer coefficient (W/m^2 K)
J	phase superficial velocity (m/s)
k	thermal conductivity (W/m K)
ℓ	length specified in image (m)
L	length of the channel, characteristic length (m)
m	ratio of relative bubble velocity to bubble velocity (−)
N	number of observed bubble
n	frames per second
p	perimeter (m)
Q	volumetric flow rate (m^3/s), heat input (W)
q''	heat flux (W/m^2)
R	radius (m)
S	slip ratio (−)
T	temperature (K)
T^*	non-dimensional temperature (−)
t	time (s), thickness (m)
U	velocity (m/s)
x	gas fraction (−)
Z	distance from inlet (m)
Z^*	thermal non-dimensional distance ($=Z/Re{\cdot}Pr{\cdot}D_h$)

Greek symbols

δ	substrate thickness (m)
β	volume flow ratio (−)
ε	void fraction (−)
η	liquid film thickness (m)
ζ	frequency of bubbles (Hz)
μ	dynamic viscosity (Pa s)
ρ	mass density (kg/m^3)
φ	heat flux ratio (−)
ψ	ratio of bubble velocity to total superficial velocity (−)
σ	surface tension (N/m)

Non-dimensional numbers

Bo	Bond number $D_h \cdot \{(\rho_l - \rho_g) \cdot g/\sigma_l\}^{0.5}$
Ca	Capillary number $(\mu_l \cdot U_b/\sigma_l)$
Nu	Nusselt number $(h \cdot D_h/k_l)$
Pr	Prandtl number $(\mu_l \cdot c_p/k_l)$
Re	Reynolds number $(\rho_l \cdot J \cdot D_h/\mu_l)$

Subscripts

b	bubble, bulk, base
f	fluid
g	gas
h	hydraulic, hydrodynamic
in	input
l	liquid
s	slug
sf	solid–fluid
tot	total
TP	two-phase
uc	unit cell
w	wall

as well as for catalytic reactors for micro-fuel processors, biological sensors, lab-on-chip devices, water management of PEM fuel cells, high heat flux dissipating heat exchanger equipment etc. Mostly in these mini/micro-scale devices, heat transfer process is conjugate in nature, i.e. the diffusion in the solid wall of the channel affects the thermal boundary condition (uniform heat flux or uniform wall temperature) which the fluid experiences at the solid–fluid interface. This conjugate nature of thermal transport increases the level of complexity in the estimation of local heat transfer, demanding an effective means of accurate non-intrusive field measuring instruments as against intrusive point measurements, such as by micro thermocouples (Majumder et al., 2013). In this context Infra-Red Thermography (IRT) has emerged as an effective non-intrusive field measurement technique in the recent past (Hetsroni et al., 1996, 2003) to address the local measurement of a variety of complex problems involving high spatial temperature gradients. In the present work, we have made an attempt to estimate the local heat transfer coefficient under such demanding conditions involving (i) Intermittent Taylor bubble train flow, (ii) non-circular (square) mini-channel, by employing non-intrusive field measurement by InfraRed Thermography. The paper presents an experimental design methodology so that local heat transfer can be estimated by minimizing the conjugate heat transfer effects in the system. As will be revealed in the survey of open literature, which is presented in the subsequent section, understanding of local species transport under such flow conditions is quite an involved problem.[1]

[1] It must be noted here that the issue of accurate experimental measurement of the bulk mean-mixing temperature of the respective fluid-phases, under such intermittent flow conditions, is not trivial. The procedure adopted in this work to estimate this temperature requires further refinement (refer Section 3.3). Other major aspects towards estimating the correct local heat transport parameters have been included in the design of the experiment presented here.

2. Literature review

In one of the seminal works on Taylor bubble flows, it was observed that a bubble does not rise spontaneously in a water filled vertically oriented circular capillary under the effect of gravity for $Bo < 1.835$ (Bretherton, 1961) and film thickness scaling was found as $(\eta/R) \sim Ca^{2/3}$, valid for $10^{-3} \leqslant Ca \leqslant 10^{-2}$. Deposition of thin liquid film due to displacement of the wetting fluid by a gas bubble inside a circular capillary wall has been studied (Fairbrother and Stubbs, 1935) and another scaling for film thickness was given as $(\eta/R) \sim Ca^{1/2}$ for $10^{-5} \leqslant Ca \leqslant 10^{-1}$. Under Taylor bubble train flow conditions, the bubble velocity will not be equal to the liquid due to the existence of liquid film that separates the bubble from the wall (Fabre and Liñe, 1992; Thulasidas et al., 1995, 1997). Presence of bubble interfaces at front and back of the liquid slugs modifies the flow field inside it. Circulation takes place inside the liquid slug due to existing wall shear stress, which in turn enhances the species transport. It has been hypothesized that for low Ca, circulation patterns in the liquid slug will be observed with paired set of vortices, which tend to disappear for higher Ca, leading to bypass flows (Taylor, 1961). More recent numerical and experimental studies (Taha and Cui, 2004, 2006; Kashid et al., 2005; He et al., 2010; Bajpai and Khandekar, 2012) have confirmed these findings. In recent years focus on Taylor bubble flows in non-circular channels has also attracted attention. Shape of the bubble cross-section in a square capillary has been experimentally determined and it is concluded that for $Ca \leqslant 0.1$, bubble cross-section is non-axisymmetric. As the total superficial velocity increases and Ca becomes greater than 0.1, the increased inertia forces tend to make the bubble cross-section axisymmetric (Kolb and Cerro, 1993; Han and Shikazono, 2009). Numerical study of the flow of long bubble in a square capillary suggested that liquid deposition on capillary wall is a function of flow Ca (Kamisli, 2003). Flow pat-

tern transition and frictional pressure drop has been investigated in different rectangular channels, and correlations to predict them, including the Chisholm's factor (estimates the slip ratio S, based on annular flow model, defined as: $S = \sqrt{1 - x(1 - \rho_l/\rho_g)}$, where x is quality of gas-phase), have been reported (Ide and Matsumura, 1990; Mishima et al., 1993; Chen et al., 2009).

Study of heat transfer in gas–liquid two-phase flow revealed higher heat transfer coefficient than equivalent single-phase flows. Very small temperature gradient exists beneath the bubble which enhances the heat transfer whereas in the liquid slugs, existence of circulating flow due to presence of bubble interfaces at front and back enhances local heat transfer (Bao et al., 2000; Fukagata et al., 2007; Narayanan and Lakehal, 2008; Gupta et al., 2010). Experimental investigation of heat transfer in non-boiling two-phase slug flow in a circular channel of diameter 1.5 mm using InfraRed Thermography (IRT) has been reported by Walsh et al. (2010). Similar study using micro-thermometry in non-circular (square) mini-channel of $D_h = 3.3$ mm has been recently done by Majumder et al. (2013). Both studies reveal that such flows can be highly efficient in enhancement of heat transfer, as compared to fully developed single-phase flows. Several numerical studies of Taylor slug flow have also been reported in recent times which highlighted the effect of L/D, Pr, Ca, on the heat transfer and shear stress (Asadolahi et al., 2011; Bajpai and Khandekar, 2012). Detailed computational simulations, including the thin film surrounding the gas bubble, have been reported using the VOF method and an overall enhancement up to 610% in the heat transfer has been reported (Mehdizadeh et al., 2011). Simulation of a 'unit-cell' using periodic boundary condition with moving frame of reference revealed the limitations of assuming 2-D axisymmetric conditions; in reality the flow becomes three-dimensional in nature, especially for $Re_{TP} \geqslant 950$ (Asadolahi et al., 2012; Talimi et al., 2012a). Recent micro-PIV studies on circular and non-circular channels clearly reveal the flow recirculations inside the liquid slugs and the effect of gravity on film thickness and heat transfer (Leung et al., 2012; Zaloha et al., 2012). In a recent extensive review, Talimi et al. (2012b) emphasized that, looking into the design need of several upcoming engineering systems and technologies, extensive exploration of hydrodynamics and heat transfer of Taylor slug flow in the non-circular ducts, under different thermal boundary conditions must be undertaken.

As has been pointed out earlier, convective flows in mini/micro geometries are prone to the effects of conjugate heat transfer conditions within the solid substrate in which the flow takes place, affecting the overall heat transfer performance (Nonino et al., 2009; Moharana et al., 2011b). Maranzana et al. (2004) proposed a new criterion for quantifying the effect of axial conduction in mini/micro systems. Simultaneously developing single-phase laminar flow in rectangular mini-channel array was studied and it was concluded that axial conduction in the substrate becomes significant for higher values of Axial Conduction Number i.e., $M \geqslant 0.01$.

$$M = \frac{q''_{cond}}{q''_{conv}} = k_w \left(\frac{W \cdot p/L}{\rho_f \cdot C_{pf} \cdot \delta_f \cdot p \cdot u} \right) \tag{1}$$

Here, q''_{cond} gives the first-order estimation of the axial heat flux in the wall, assuming the heat transfer is one dimensional along the length of the channel through the same temperature difference which the fluid experiences between channel inlet and outlet. The parameter M allows the comparison of the axial heat transfer by back conduction in the substrate wall to the convective heat transfer (q''_{conv}) to the fluid. Naturally, if the value of M is high, axial conduction effects are important and cannot be neglected. Eq. (1) can be rewritten as:

$$M = \frac{1}{(Re \cdot Pr)} \left(\frac{D_h}{L} \right) \cdot \left(\frac{W}{\delta_f} \right) \cdot \left(\frac{k_w}{k_f} \right) \tag{2}$$

Lee et al. (2005) and Lee and Garimella (2006) conducted a 3-D conjugate laminar heat transfer analysis, including entrance effects, for single channels as well as micro-channel heat sinks, subjected to uniform heat flux imposed on the bottom of the substrate. Operating regimes and boundary conditions wherein conjugate effects become important were identified. Correlations to predict local and average Nusselt number were also proposed.

Conjugate effects during convective flows also pose challenge for designing of experimental setup for proper measurement of heat transfer coefficient. In addition, data reduction process has to be carefully addressed so that errors in estimation due to the conjugate effects do not arise. In general, the local Nusselt number gets affected by the distortion of the thermal boundary condition due to axial back conduction in the substrate/pipe/channel wall. The geometrical parameters of the channel, flow Reynolds number, the area ratio (A_{sf}) and the thermal conductivity ratio (k_{sf}) have been recognized as the primary influencing parameters in the analysis of conjugate heat transfer (Celata et al., 2006; Nonino et al., 2009; Rao and Khandekar, 2009; Moharana et al., 2012). In this context, point measurement systems such as thermocouples have obvious limitations to quantify the extent of the conjugate effects on thermal transport behavior. In such a situation therefore, complete field information is necessary to estimate the spatial temperature gradients in the wall and fluid region, a recent example of which is the use of InfraRed Thermography (IRT) for estimating local heat transfer coefficient during single-phase thermally developing flows with conjugate effects (Mehta and Khandekar, 2012).

In recent past, IRT has sufficiently evolved as a versatile technique for the measurement of heat transfer in single-phase flows, two-phase flows in micro-scale systems, high enthalpy flows, multi-jet systems, jet impingements on rotating disks, jet in cross flow, space radiator plates etc. (Hetsroni et al., 1996, 2003; Astarita et al., 2000; Hemadri et al., 2011). The limitations of the technique, including the sources of measurement errors, calibration issues, emissivity corrections, effect of participating media, noise isolation, data reduction issues have also been addressed (Sargent et al., 1998; Buchlin, 2010; Hetsroni et al., 2011).

Literature review clearly suggests that: (i) Limited studies are available on experimental investigation of heat transfer in Taylor bubble train flows in non-circular mini/micro channels. (ii) Local transport parameters are not usually addressed; at present, such information is only available in numerical simulations, most of which focus on circular channels. In addition, most experimental studies rely on point measurements. (iii) Very few studies address conjugate effects and non-standard boundary conditions in Taylor bubble train flow situations, which frequently arise in mini/micro systems. In such situations the design of experiment becomes critical.

In this work estimation of local heat transfer coefficient for Taylor bubble train flow in a square mini-channel of size 5 mm × 5 mm by non-intrusive InfraRed Thermography has been undertaken. The experimental setup design must ensure that conjugate nature of heat transfer does not adversely affect the true estimation of heat transfer coefficient for Taylor bubble train flow. The design of the experiment is addressed next.

3. Design of experiment

Before attempting to measure local heat transfer coefficient under Taylor bubble train flow situation, the experimental design must be benchmarked against single-phase flow. Most of the analytical solutions for fully-developed or developing convective

single-phase flows are available for standard boundary conditions with no conjugate effects (Shah and London, 1978). In situations where non-standard boundary conditions are applicable and/or conjugate effects are encountered, problem of estimating the heat transfer coefficient has to be either tackled through computational techniques and/or through an experimental route. If accurate heat transfer coefficient needs to be experimentally determined in a given non-standard system, the protocol must be such that conjugate effects are either (i) completely isolated or quantifiable (ii) minimized so as to ascertain the true local heat transfer coefficient.

The design procedure for the experimental setup involves several steps. Firstly, viscous dissipation in the liquid can be neglected for the range of parameters considered in this study. Secondly, while the Peclet number considered in this work are large enough to assume that the axial conduction in the fluid domain will be negligible, only the axial back conduction in the solid substrate must be minimized and quantified. Under single-phase flow conditions, guidelines for minimizing and quantifying the conjugate effects due to the solid substrate are available in the literature (Maranzana et al., 2004; Nonino et al., 2009; Moharana et al., 2011b). As discussed earlier, guidelines provided by the axial conduction number M provides the first-order working guideline for designing systems with minimal effects of axial back conduction in solid substrates. A low value of M is desirable, which ensures that axial conduction in the substrate will not affect the nature of boundary condition experienced by the fluid at the fluid–solid interface. This has been achieved in the present setup by employing computational simulation of heat and fluid flow through iterative design procedure, the nuances of which will be described in Section 3.2. The final geometrical parameters of the experimental setup, as described next, evolved as a result of the computational design simulations.

3.1. Description of the experimental setup

Schematic details of the experimental setup are shown in Fig. 1(a–d). The heated test section consists of a single square mini-channel with cross section area = 5 mm × 5 mm, D_h = 5.0 mm, machined on a stainless steel substrate (k = 16 W/m K; k_{sf} = 25; M = 0.0014), dimensions of which are 300 mm × 25 mm × 11 mm. The basis of these dimensions will be scrutinized in Section 3.2. In the upstream direction of the heated section, there is a 300 mm visually transparent unheated channel length of polycarbonate material which is provided for the complete hydrodynamic flow development in the entire range of Re applicable to the single-phase flow experiments. Two-phase Taylor bubble train flow (degassed and deionized water as liquid-phase and dry air as gaseous-phase) is generated with the help of an air injection system (T-junction) located far upstream. In the present case, both the connectors/arms constituting the T-junction have exactly the same cross-section, i.e., square section of size 5 mm × 5 mm. Constant temperature bath (Make: Julabo® F34 ME, precision ± 0.1 K) is used to supply the water and dry-air is supplied from a pressurized cylinder through the T-junction (Fig. 1). In the case of Taylor bubble train flow, the unheated length provides necessary flow stabilization after air bubbles get formed at the T-junction. In addition, it is also used to visualize the Taylor bubbles before they enter the heated test section. This visualization has been done by using Photron-Fastcam®-SA3 high speed camera. Image acquisition has been done at 500 fps for all the Taylor bubble train flow experiments. It must be noted here that the design of the T-junction (which includes diameter ratio of liquid supply arm to that of the gas supply arm, internal edge geometry, wettability of the material, etc.) determines the resulting bubble patterns formed by it.

Fluid temperature at inlet (T_{fi}), outlet (T_{fo}) and at three other locations (T_{f1}-T_{f3}) in the heated test section have been measured by suitably located K-type micro thermocouples (Omega®, 0.13 mm bead diameter, precision ± 0.1 after calibration), as shown in Fig. 1(a) and (c). The time constant of these thermocouples are of the order of 10^{-4} s, which ensured sufficient dynamic response. In addition to these five thermocouples for fluid temperature measurement, three more K-type pre-calibrated thermocouples T_{w1}-T_{w3} are embedded in the wall of the heated test section, as detailed in Fig. 1(a) and (c). All thermocouple data acquisition has been carried out at 30 Hz by using a high precision 24 bit PCI-DAQ card

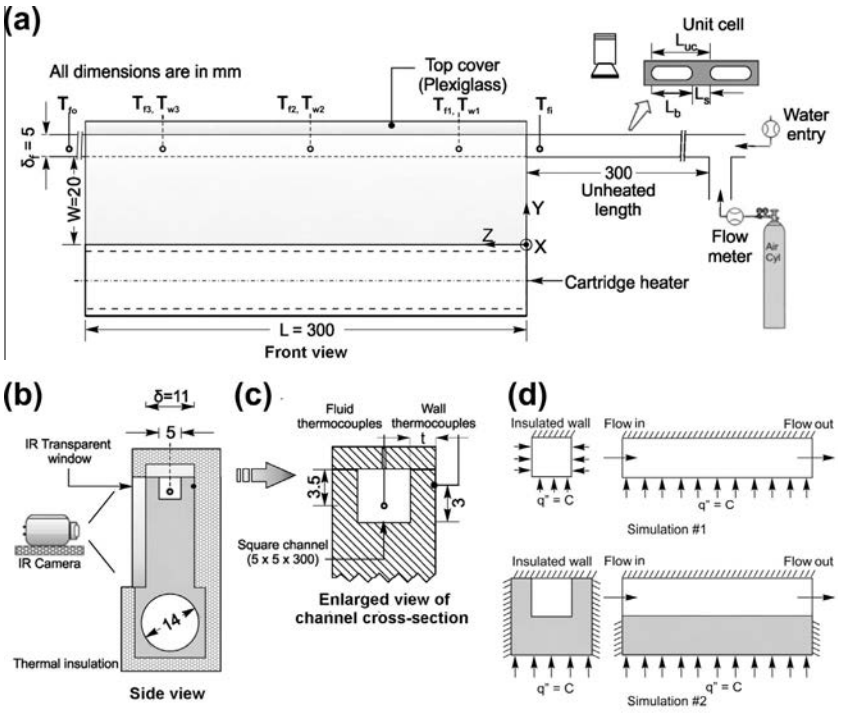

Fig. 1. Schematic details of the experimental test setup.

(Make: National Instruments®, NI 9213). All thermocouples are calibrated against standard Pt-100 NIST traceable thermocouple.

The cylindrical DC supplied cartridge heater is located away from the actual fluid–solid interface, as shown. Precise digital multi-meter (precision ± 0.1 V and ± 0.01 A) is used to measure the electrical power dissipation of the heater. Necessary insulation is provided to the entire setup by plexi-glass/foam blocks, including the top of the channel, as shown. Apart from the standard energy balance technique, heat losses were also estimated by conducting the experiments in the no flow condition for different heat inputs, respectively, and recording the steady-state IR thermogram and wall thermocouple temperature. In such a condition, whatever heat was supplied to the system got dissipated to the environment. Therefore, different values of average surface temperature corresponding to the different heat inputs have been obtained and used for estimating heat lost during the actual experiments. With both these complementary methodologies, it was found that the maximum losses never exceeded 8% - 11% of the gross input.

The IR camera used (Make: FLIR®, Model: SC4000; Indium Antimonide detector array) has an operational spectral band of 3–5 μm, 14 bit signal digitization and a Noise Equivalent Temperature Difference of less than 0.02 K at 30 °C. As shown in Fig. 1, the spatial temperature field of the front side of the substrate having an area 25 mm × 290 mm is captured by the IR camera. A very thin uniform spray coating of high emissivity black paint (Make: Nextel® $\varepsilon > 0.95$) has been done on this side to ensure reliable IR measurements. Apart from this, the experiment has been set-up in a dark room with non-reflecting background to minimize the surrounding radiation. As the maximum Biot number in the X-direction based on the channel wall thickness, t ($Bi = ht/k_w$), is of the order of 0.09 (< 0.1), lumped assumption will hold and temperature gradient in that direction will be negligible. The recording of spatial IR thermographic profiles of the front surface of the substrate is facilitated by a 5 mm thick InfraRed transmitting CaF_2 glass window (Make: Crystran®; Transmissivity: 95%, for wavelength 2 μm - 7 μm; Refractive index = 1.399 at 5 μm; $k = 9.71$ $Wm^{-1}K^{-1}$). IR images have also been acquired at 30 Hz and post processed by using ThermaCAM™ Researcher-V2.9 software. IR thermograms are captured at 320 pixels × 256 pixels which give a spatial resolution of 900 microns in the Z-direction and 750 microns in the Y-direction. While the software incorporates protocols for corrections due to ambient temperature, ambient humidity and absorptivity of the medium, local emissivity of the target must be supplied by conducting in situ calibration against standard temperature measurement technique. Before conducting the experiments, the text assembly (including the CaF_2 glass window) was calibrated in the entire range of operating temperatures by simultaneous measure of surface temperature by a NIST traceable Pt-100 thermocouple and IR camera. The emissivity matrix thus generated was supplied to the software for post processing to get the correct temperature field. In addition, during the experiments, as has been described earlier, four thermocouples were always kept for referencing. Several independent benchmarking and validation experiments for precise calibration of the camera were also conducted, as detailed in Mehta and Khandekar (2012).

3.2. Computational design procedure

To evolve the design of the above experimental setup and to undertake benchmarking of the data, 3-D computational simulations of single-phase laminar flow were first carried out on ANSYS®-Fluent, on two separate geometries, as detailed in Fig. 1(d). In Simulation #1, fluid flow and heat transfer is studied in a square channel, uniformly heated from three sides while the top side is kept insulated, i.e., no conjugate effects are taken; the governing equations for fluid flow and heat transfer are only solved in the fluid domain. Thus, Simulation #1 serves as a benchmark for the non-conjugate situation. Simulation #2, on the other hand, depicts the current experimental situation wherein the conjugate heat transfer problem is solved taking the heat flow through the solid substrate domain also. Here, heat flux is applied at the bottom of the solid substrate (representing the heater, as done in the experiment), which is located away from the solid–fluid boundary, while all other side walls were kept insulated, as shown. The geometrical, thermophysical and flow parameters, for example, the length L, the width W, the thermal conductivity of the substrate k_w, and flow Re were varied to obtain different range of the axial conduction parameter M, on the conjugate physical domain, as depicted in Fig. 1(a) and (b). Flow conditions in both the simulations are kept hydrodynamically fully developed and thermally developing i.e., Graetz type flow, exactly as per the experimental conditions. Both simulated geometries correspond to channel cross-section = 5 mm × 5 mm and inlet Prandtl number is kept constant = 5.0, corresponding to water. Computational domains depicting these geometries were created using hexahedral grid system on Gambit® 2.3. The flow Re was changed so that the axial length L of the channel will cover the entire range from thermally developing to thermally fully developed conditions at the exit. The complete problem formulation, including the details of the conservation equation for mass, momentum and energy, as applicable to both the cases, numerical schemes to solve the governing equations and grid independence has been discussed in detail in Mehta and Khandekar (2012), and therefore, not repeated here for brevity.

The primary result of interest, in the context of the present experimental setup, is as shown in Fig. 2(a–d), wherein the axial variation of wall and bulk mean mixing fluid temperature profile, respectively, and the heat flux ratio, φ, at solid–fluid interface is plotted based on A_b. Heat flux ratio φ is defined as the ratio of the local heat flux q''_z, experienced by the fluid at any location on the solid–fluid interface to that of the applied constant heat flux q'' at the bottom of the substrate by the heater, i.e., $\varphi = q''_z/q''$. For Simulation #1 φ is always = 1 while for Simulation #2, φ will vary depending on the parameter M and ratio of the base area ($A_b = 3300$ mm^2) to the solid–fluid interface area ($A_{sf} = 4500$ mm^2). Reported simulations are for $Re = 200$ and $Re = 500$ respectively, with the length of the channel kept sufficiently long for complete thermal boundary layer development ($Z^* = 0.25$). As the flow enters the channel, it starts to develop thermally, eventually reaching fully developed conditions at the exit of the channel. As can be seen, parametric variation of axial conduction number M has a strong influence on the wall temperature, fluid temperature as well as the local value of heat flux ratio. Low values of M ($M < 0.01$) ensured that the fluid temperature rise is nearly linear (Fig. 2(a) and (c)); clearly indicating that the heat flux experienced by the fluid is constant throughout the channel, as seen in Fig. 2(b) and (d). Also, the wall temperature variation is as per the standard trend applicable for constant heat flux systems i.e., in the thermally developing zone, wall temperature will be nonlinear and as flow approaches to developed flow, it increases linearly (as obtained from Simulation #1). Moreover, the difference between the wall and fluid temperature becomes constant for the rest of the downstream locations. As is clearly observable, results from Simulation #2 nearly overlap those from Simulation #1 for $M < 0.002$, which forms the basis of selecting $M = 0.0014$ for the present experimental conditions. Thus, the choice of parameter M for the present experiments is dictated by two primary considerations (i) sufficient frontal area must be available so as to get good spatial resolution of thermographic data and, (ii) conjugate effects must also be simultaneously minimized.

In contrast, as the value of parameter M increases ($M > 0.01$), a noticeable change in the heat transfer behavior is observed. Firstly, the local heat flux at the fluid–solid interface does not remain

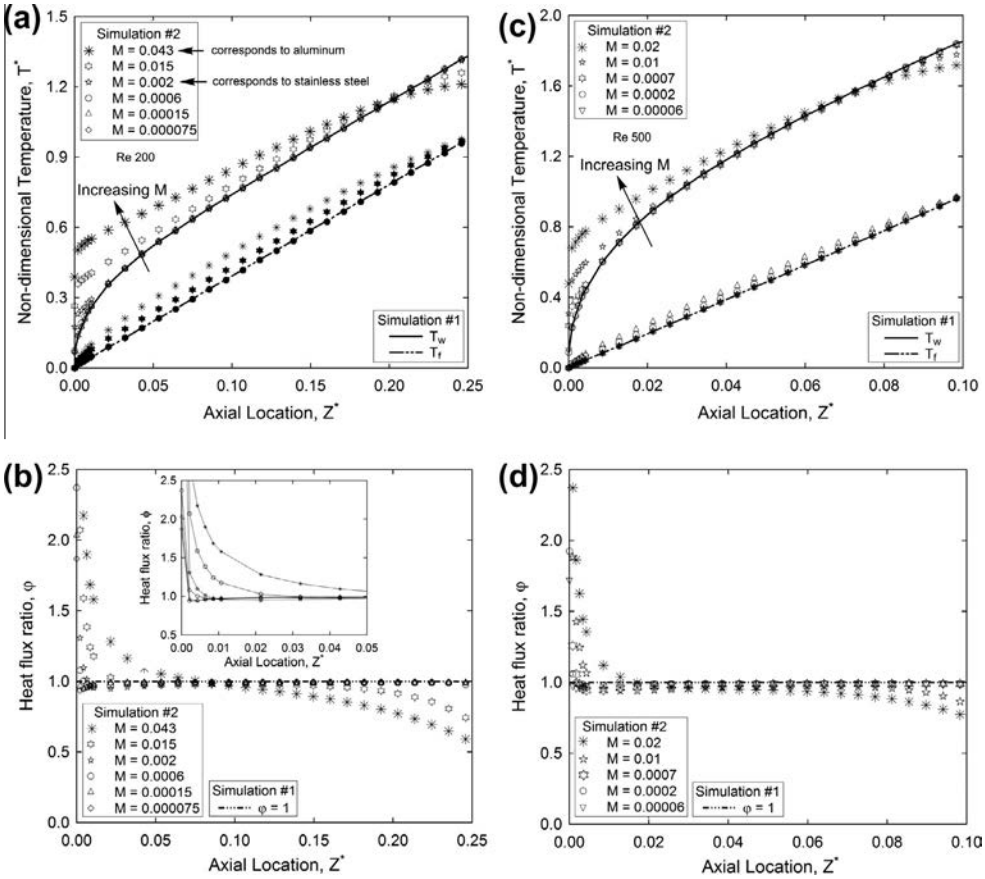

Fig. 2. Axial variation of temperature profile and heat flux ratio for Re = 200 and 500.

constant due to axial back conduction in the solid substrate from the downstream location towards the upstream sections. This causes the axial variation of fluid temperature to become non-linear. The backward movement of heat in the substrate also causes the wall temperature at the upstream location to rise, with simultaneous decrease of wall temperature in the downstream side. Thus, the constant heat flux boundary condition applied away from the fluid–solid interface seems to get severely distorted as the value of M increases beyond a particular limit.

As was described in the earlier section, for the present experiment, the value of M was equal to 0.0014, an order of magnitude lower than what is suggested by the computational simulations for avoiding the conjugate heat transfer. This therefore ensured that (i) Sufficient area was available to capture the temperature isotherms so that a good estimate of the local spatial gradients could be obtained and, in addition, (ii) the axial conduction in the substrate had minimal effect on the estimation of heat transfer coefficient obtained by the data reduction scheme, as outlined next.

Fig. 3 further scrutinizes the experimental design, wherein extended data has been provided at Re = 200, complementary to that of Fig. 2(a) and (b). Fig. 3(a) shows the computationally obtained non-dimensional temperature profile along the X-direction at three different Y-locations represented by lines L-1 to L-3 (see inset), respectively, as shown. It can be clearly seen that temperature gradient in the channel wall along the X-direction (transverse to the flow) is rather small (less than $\sim$ 0.4 °C). This supports the premise of the design that the surface temperature obtained by IR is a fairly good representative of the fluid–solid channel wall temperature.

Looking at Fig. 3(b), which shows the temperature contour of a XY plane at Z = 150 mm, it can also be noted that, below the channel bottom, practically no temperature gradient $\partial T/\partial X$ exists in the solid substrate domain (along the line L-1). This is the zone where the experimental heat flux based on A_b is proposed to be estimated by a one-dimensional heat transfer assumption (see Section 3.3, Fig. 4). The near one-dimensional nature of Y-directional heat flow in this zone validates the IR based measurement scheme. Fig. 3(c) shows the axial variation of computational and experimental heat flux ratio, on the basis of A_b (Simulation #1) and A_{sf} (Simulation #2). It can be seen that heat flux is approximately constant along the flow direction, as required by the design. Fig. 3(d) and (e) shows the temperature contour and contour of $\partial T/\partial X$ at the XZ plane located at Y = 22 mm. Here, it can be seen that for M = 0.0014 (current experimental setup), the thermal boundary condition at solid–fluid interface is maintained to be near constant heat flux. This can be clearly inferred from the fact that at particular X-location, $\partial T/\partial X$ is constant along the Z-direction. These simulations thus confirm that the experimental design is efficient in providing uniform heat flux along the flow direction (Z-direction) while the transverse temperature gradient across the X-direction is sufficiently small.

3.3. Data Reduction

Non-dimensional temperatures and Nusselt number are defined as:

$$T^* = \frac{T - T_{fi}}{(Q_{in} \cdot D_h)/(A_{sf} \cdot k_f)} \tag{3}$$

$$q''_z = -k_w (\partial T/\partial y)_z \tag{4}$$

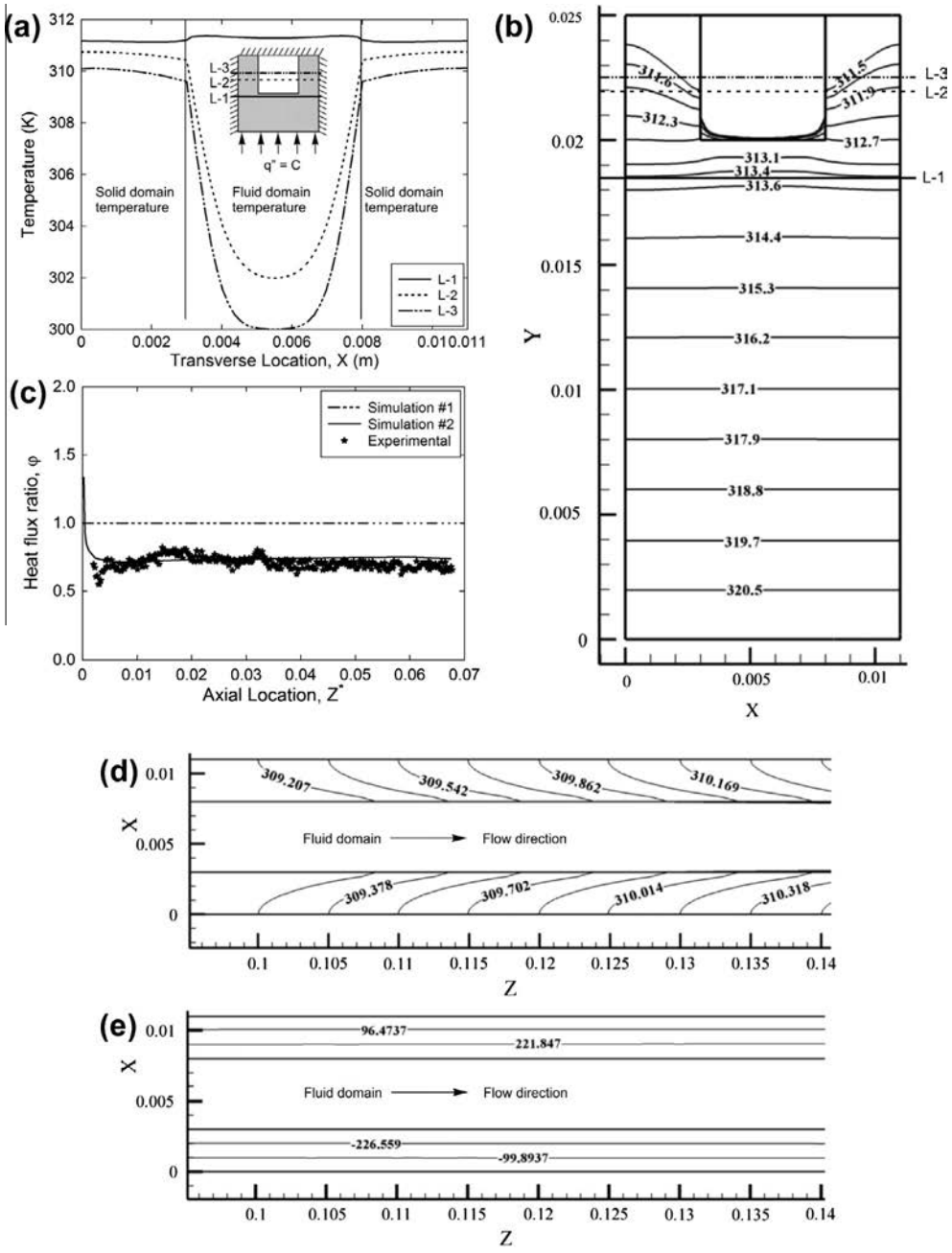

Fig. 3. (a) Wall Temperature variation across the thickness (*X*-direction) for *Re* = 200. (b) Temperature contour of central plane (*Z* = 150 mm) across the thickness for *Re* = 200. (c) Axial variation of heat flux ratio estimated for heated area for *Re* = 200. (d) Temperature contour of plane (*Y* = 22 mm) along the *Z*-direction for *Re* = 200. (e) Contour of $\partial T/\partial X$ along Z-direction for *Re* = 200.

$$Nu_z = \frac{q''_z \cdot D_h}{(\bar{T}_w - \bar{T}_f) \cdot k_f} \tag{5}$$

Local heat flux q''_z is calculated from experimentally obtained IR thermograms, as explained in Fig. 4.

3.3.1. For experimental data reduction

$\bar{T}_w$ = local wall temperature at any given location along the *Z*-axis, averaged along the direction of *Y*-axis, over the front face of the channel wall, as shown in Fig. 4.

It will be appreciated that there is no straight-forward experimental way to determine the bulk mean mixing temperature of the fluid $\bar{T}_f$. From an experimental point of view there are two possibilities, either to use:

(a) $\bar{T}_f = \bar{T}_{f-th}$ = local fluid temperature measured at point by embedding a thermocouple in the channel cross section along the streamwise direction. In the present experiment this has been done by placing five thermocouples, located as shown in Fig. 1(c). However, this is not the true representation of the bulk mean mixing temperature of the fluid.

or

(b) $\bar{T}_f = \bar{T}_b$ = local bulk mean mixing fluid temperature based on heat balance, assuming that constant heat flux is maintained throughout the length of the channel, at the fluid–solid interface. This is adopted by most researchers, in the absence of any other means of estimation.

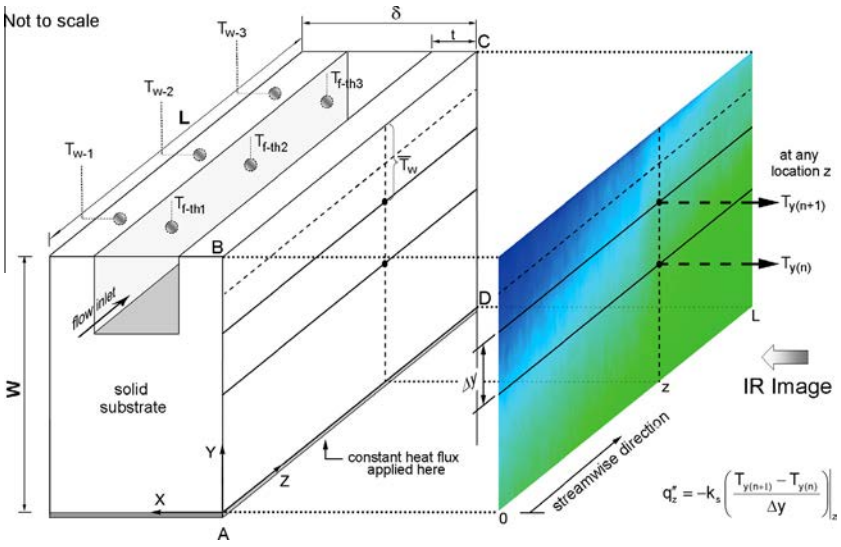

Fig. 4. Schematic explaining the estimation of local heat flux using 1-D conduction approximation from IR thermogram (Mehta and Khandekar, 2012).

For the present experiments too, both the methodologies have been adopted for data reduction and comparison. For each experimental run, time-averaged wall and fluid temperatures, $\bar{T}_w$ and $\bar{T}_f(=\bar{T}_{f-th})$, respectively, are numerical estimated from the local thermocouple data integrated over 60 s (at 30 Hz we get 1800 data points), after quasi-steady state is achieved. In addition, each experimental run also provides an estimate of bulk mean mixing temperature $\bar{T}_f = \bar{T}_b$. As will be demonstrated and discussed later, this latter approach can lead to serious errors in the estimation of Nusselt Number, especially when conjugate effects are predominant and/or parameter M is large.

3.3.2. For numerical data reduction

$\bar{T}_w$ = local peripheral averaged heated wall temperature, at the fluid–solid interface, at any given location along the Z-axis.

$\bar{T}_f = \bar{T}_b$ = local bulk mean mixing fluid temperature at the fluid cross-section of interest along the channel, as obtained from the simulation.

Mean bubble velocities are calculated from digital analysis of image obtained from high speed videography. As image acquisition rate is known, bubble velocity can be ascertained. If N is the number of bubbles tracked for estimating the average bubble velocity U_b, n represents the fame rate of video capture, ℓ represents the length of the observation window and Δf is the number of frames required for a bubble to pass through the window, then:

$$U_b = \frac{1}{N}\sum_{i=1}^{N}\left(\frac{\ell}{\Delta f}\right)_i n \tag{6}$$

For the present range of experiments, values chosen for estimation of average bubble velocity U_b are $N = 20$, $n = 500$ frames/s and $\ell = 10$ mm. Sequence of images also provides us the average time required for the unit cell to pass through a fixed observation point, t_{uc}. This provides the necessary bubble frequency, given by:

$$\zeta = (1/t_{uc}) \tag{7}$$

In the present experimental measurements, variations in the bubble/liquid slug lengths and velocities are not more than ±3%. Present calculations have been shown in Table 1, along with the definitions used. Taylor bubble flow hydrodynamics is completely described by making the length of a unit cell ($L_{uc} = L_b + L_s$) as the basis.

4. Results and discussion

4.1. Benchmarking with single-phase experiments

First, benchmarking of the experimental setup has been done by conducting heat transfer experiments in laminar single-phase flow and results are validated with its corresponding numerical simulations. Several test runs were conducted and the axial variation of heat flux ratio, non-dimensional average wall temperature, fluid temperature and the local Nusselt number at the solid–fluid interface are obtained and shown in Fig. 5(a–c).

Fig. 5(a) shows the experimentally obtained axial variation of heat flux ratio at solid–fluid interface, as estimated from Eq. (4), compared against results obtained from Simulation #1 ($M \sim 0$) and #2 (with $M = 0.0014$). It is important to note that this data is same as shown in Fig. 3(c) but its representation is different because here, heat flux has been calculated on the basis of base area ($A_b = 3300$ mm^2) just to show the overall energy balance. The scatter in the experimental data is for three independent experimental runs done for flow $Re = 200$. Very similar scatter was obtained for tests done at other flow Reynolds numbers ranging from 150 to 500. The corresponding IR thermogram obtained at steady-state is shown in Fig. 5(e). As can be seen, the design of the experiment not only provides sufficient spatial resolution for obtaining temperature gradients from the thermograms but also minimizes the effect of axial conduction on the heat flux values experienced by the fluid. The fluid experiences near constant heat flux throughout the axial length of the channel. Due to this favorable design conditions, the comparison of the axial variation of wall temperature, as shown in Fig. 5(b) is also quite satisfactory.

The experimental fluid temperature, as measured by the five thermocouples, protruded in the channel cross-section (as detailed in Fig. 1(c)), comes out to be lower than the bulk mean mixing temperature. As discussed earlier, the thermocouples only provide local point temperature of the thermal boundary layer, at the location where they have been fixed. For the present experiment, this measured point temperature is lower than the bulk mean temperature of the fluid. The 3-D numerical simulations also provide the data for the temperature at the exact location of the thermocouple, which matches very well with the experimental fluid temperature $\bar{T}_f = \bar{T}_{f-th}$. The comparison of local fluid temperature (as obtained from the experiment as well as Simulation #2) and bulk mean mixing temperature (as obtained from Simulation #2) is also tabulated in Fig. 5(d).

Table 1
Experimental results of Taylor bubble train flow from image analysis.

β (Re_{TP})	Ca	J_g (m/s)	J_l (m/s)	J_{tot} (m/s)	$\psi = U_b/J_{tot}$	U_b (m/s)	L_s (mm)	L_b (mm)	ζ (Hz)
0.384 (430)	0.0009	0.033	0.053	0.087	0.85	0.074 ± 0.002	22.63 ± 1.02	15.95 ± 0.60	1.92 ± 0.05
0.552 (600)	0.0013	0.067	0.053	0.120	0.88	0.105 ± 0.003	17.72 ± 0.87	18.61 ± 1.16	2.43 ± 0.03
0.652 (760)	0.0020	0.100	0.053	0.153	1.02	0.156 ± 0.002	6.80 ± 0.32	26.32 ± 0.48	4.85 ± 0.04
0.714 (930)	0.0024	0.133	0.053	0.187	1.01	0.188 ± 0.006	6.43 ± 0.61	31.16 ± 0.79	5.16 ± 0.02

$\beta = Q_g/(Q_g + Q_l)$; $J_g = Q_g/A$; $J_l = Q_l/A$; $J_{tot} = J_g + J_l$; $\psi = (U_b/J_{tot}) = (\beta/\varepsilon)$.

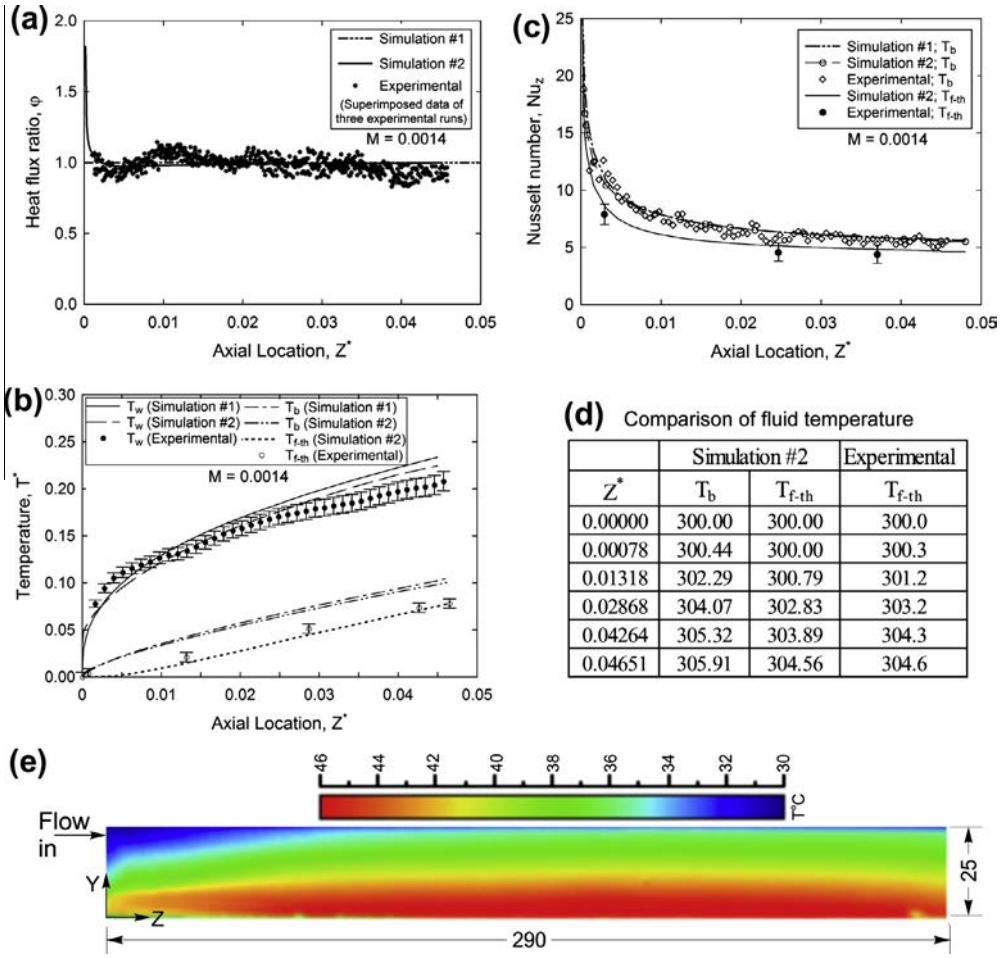

	Simulation #2		Experimental
Z^*	T_b	$T_{f\text{-}th}$	$T_{f\text{-}th}$
0.00000	300.00	300.00	300.0
0.00078	300.44	300.00	300.3
0.01318	302.29	300.79	301.2
0.02868	304.07	302.83	303.2
0.04264	305.32	303.89	304.3
0.04651	305.91	304.56	304.6

Fig. 5. (a) Axial variation of heat flux ratio at solid–fluid interface, (b) axial variation of non-dimensional wall and fluid temperature, (c) axial variation of Nusselt number, (d) fluid bulk mean temperature and thermocouple temperature and (e) IR Thermogram of exposed wall for $Re = 200$.

Based on the local temperature data, axial variation of Nusselt number can now be obtained, as depicted in Fig. 5(c), as estimated from Eq. (5). Firstly, it is noted that the Nusselt number variation for Simulation #1 and Simulation #2 is nearly identical, with maximum variation of less than 5%. Thus, it is again confirmed that axial conduction has minimal effect on the estimation of local heat transfer coefficient. In addition, as has been noted in Section 3.3, experimental estimation of local Nusselt number can be done in two ways, as plotted in Fig. 5(c). This is also reflected in the experimental values based on bulk mean mixing temperature, which match well with the simulations, as the heat flux achieved in the experiments is also nearly constant. As the local fluid temperature measured by the thermocouples is lower than the bulk mean temperature estimated from the heat balance, the corresponding Nusselt number for the former case comes out to be lower than the latter.

After completing the validation of the experimental setup and gaining confidence in the experimental procedure and data reduction technique, Taylor bubble train experiments have been carried out.

4.2. Taylor bubble train flow

Taylor bubble train flow is achieved by injecting metered amount of clean air from the air cylinder at *T*-junction, which is located far upstream (300 mm) from heated section. In all the experiments reported here, the inlet liquid flow Reynolds number is kept constant = 200, based on liquid superficial velocity. The flow rate of the air, and therefore its volume flow ratio (β = the ratio of air flow rate to the total flow rate of air and water) is controlled. Results reported here are from experiments carried out at different β (from 0.384 to 0.714) by changing the air flow rate.

Fig. 6 shows the temporal variation of the fluid and wall temperature at the measurement station 1, 2 and 3 (at 325 mm, 485 mm and 575 mm from the *T*-junction) for a volume flow ratio, $\beta = 0.384$ and 0.652, respectively. Thermocouple data acquisition

has been done at 30 Hz to resolve the temporal temperature variations expected due to intermittent bubble train, which has maximum frequency not exceeding 5 Hz. As soon as the Taylor bubble train reaches the thermocouple measurement stations, it causes the wall temperature to decrease at all these locations, respectively. Simultaneously, an increase in the local fluid temperature is also noted. This increase of fluid temperature can be explained by clear indications available in the literature which suggest that such flow conditions lead to toroidal vortices in the liquid slug which enhance mixing (Taylor, 1961; Thulasidas et al., 1997; Zaloha et al., 2012; Bajpai and Khandekar, 2012). In addition, for a fixed heat input per unit length of the channel, the reduction of mean thermal capacity due to air injection, leads to a higher overall fluid temperature. The alternating pattern of liquid slug and bubble flow renew the thermal boundary layer every time the bubble passes. As can be seen in the figures, the wall and fluid temperatures again approach the original single-phase steady state values, once air injection is stopped.

The fluid temperature also fluctuates quasi-periodically due to the intermittent nature of the flow with a dominant frequency which matches with the bubble flow time scale measured from video images. Fig. 7 shows the power spectrum for the time–temperature data of fluid thermocouple data of Fig. 6; the inset images show the corresponding bubble shapes and slug lengths. The bubble frequency estimated from Eq. (7) by video image analysis, as listed in Table 1, satisfactorily matches the frequency of fluid temperature fluctuations obtained by the thermocouple. The *T*-junction for creation of Taylor bubble train functioned satisfactorily with minor scatter in the obtained slug lengths. Fig. 8 shows the thermogram and axial variation of wall temperature for different volume flow ratio. It is observed that for all volume flow ratios the corresponding wall temperatures are lower than the steady single-phase flow. Corresponding fluid temperatures, as noted in Fig. 6 were also higher. This clearly suggests an enhancement in the heat transfer due to the Taylor bubble train flow.

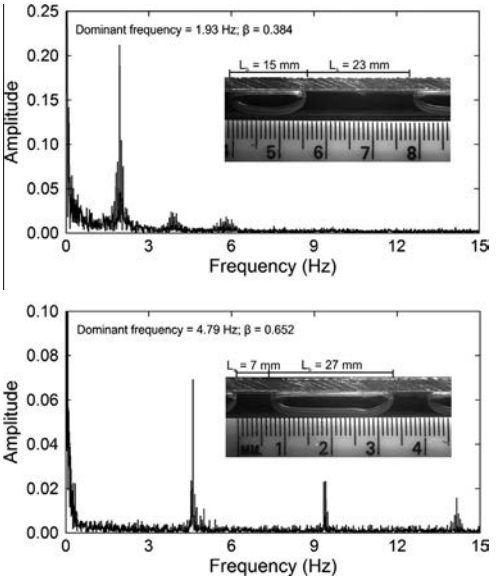

Fig. 7. Bubble frequency analysis of temperature data for $\beta = 0.384$ and 0.652.

Axial variation of time averaged Nusselt number (Nu_z), estimated at the three measurement stations, for various volume flow ratio (0.384, 0.552, 0.652 and 0.714) are superimposed on the single-phase results (experimental as well as simulation) of Fig. 5(c) and shown in Fig. 9. Corresponding typical lengths and shapes of the bubbles and liquid slugs are also shown in the inset. Particularly for Taylor bubble train flow data, the total superficial velocity (J_{tot}) represents the relevant velocity scale. Thus, the Re_{TP} values reported in Table 1 against β are based on J_{tot}. For this data set, the streamwise locations are therefore normalized by using Re_{TP}.

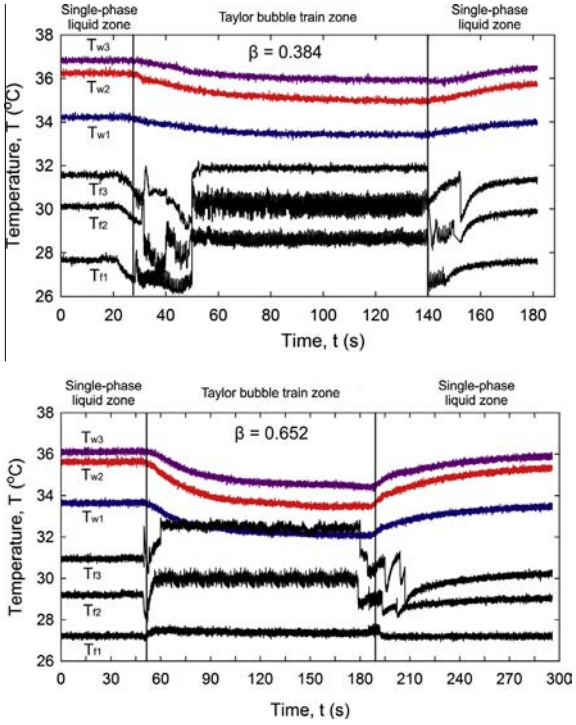

Fig. 6. Variation of wall and fluid temperature with time for Taylor bubble train flow for $\beta = 0.384$ and 0.652.

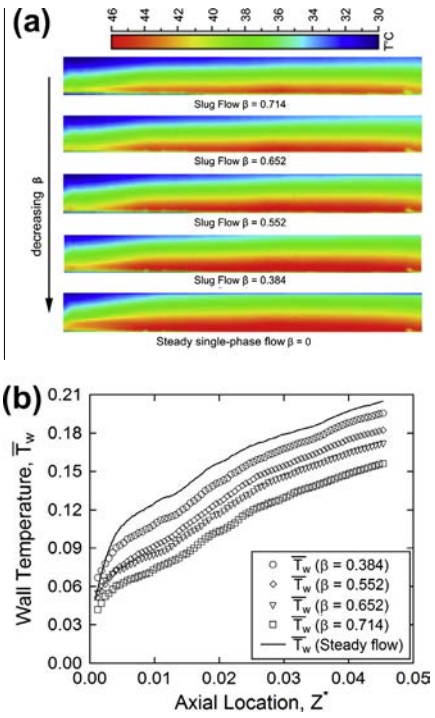

Fig. 8. (a) IR thermograms of the front exposed wall and, (b) corresponding axial variation of average wall temperature for $\beta = 0.384$, 0.552 0.652 and 0.714.

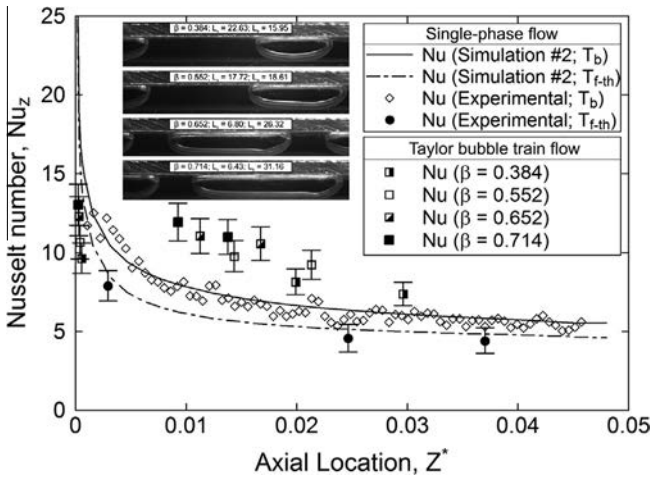

Fig. 9. Axial variation of time averaged local Nusselt at various volume fractions $\beta = 0.384$, 0.552 0.652 and 0.714.

It is clear from the results that there is significant enhancement of local Nusselt number for the Taylor bubble train flow, typically 1.2–2.0 times as compared to fully developed single-phase flow. It is also evident that for the present range of volume flow ratios used, Nu_z increases with increase of β. This happens because, as seen in the inset of Fig. 9 and noted in Table 1, as β increases, the liquid slug length trapped between the Taylor bubbles goes down. In addition, bubble velocity, U_b increases with β leading to smaller recirculation times of the fluid in Taylor slugs, contributing to heat transfer enhancement (Thulasidas et al., 1997; Walsh et al., 2010; Bajpai and Khandekar, 2012). The heat transfer enhancement with respect to the single-phase flow is not appreciable close to the channel entrance; here, due to the thermal entry length, the developing nature of the single-phase flow itself provides sufficiently high transport coefficient. In the downstream locations advantage of injecting Taylor bubbles is indeed unambiguous. Also, it is clear that axial variation of Nusselt number obtained in Taylor bubble train flow is more uniform throughout the channel, as against single-phase developing flow. This behavior is attributed to faster development of thermal boundary layers in the liquid slugs and thinner boundary layers due to the toroidal vortices, as recently highlighted by Walsh et al. (2010).

The local time averaged Nusselt number obtained for Taylor bubble train flow in Fig. 9 is based on thermocouple fluid temperature. Even if the axial heat input is constant, given the intermittent flow condition and large difference in thermal capacity of the two phases, it is quite difficult to estimate the bulk mean mixing fluid temperature in Taylor bubble train flow by the heat balance technique, as was possible in the single-phase flow situation. It is even more difficult to measure the bulk mean mixing fluid temperature at a cross-section with intrusive methods. Non-intrusive methods such as particle image thermometry or fluorescence thermometry may provide this data, however it requires elaborate methodology (Dabiri, 2009). For the present experiments, the reported enhancement in heat transfer is indeed conservative as the bulk mean mixing fluid temperature is likely to be closer to the local thermocouple reading due to enhanced mixing characteristics of Taylor slugs.

5. Summary and conclusions

An attempt has been made to measure the local heat transfer coefficient during Taylor bubble train flow by InfraRed Thermography. The issues and challenges in designing an experimental setup to achieve this goal are delineated, two major issues being (i) the setup design must provide sufficient spatial resolution for temperature field data so that local gradients can be accurately estimated and, (ii) simultaneously, the conjugate effects, if occurring in the channel must be eliminated or quantified. The presented design achieves these two objectives. If these issues are addressed, non-intrusive IR Thermography is an attractive technique to measure heat transfer coefficients, especially under (a) non-standard boundary conditions, and, (b) non-circular channels, where peripheral gradients of temperature may also exist, where non-intrusive field information is needed. Proper care is needed for data reduction so that estimates of heat transfer coefficients are meaningful. In this context, the estimation technique of the mean mixing fluid temperature is important and care must be taken to ensure that intended boundary conditions are indeed occurring at the fluid–solid interface. Prior to conducting Taylor bubble flow experiments, thorough benchmarking and validation of the setup design has been done with single-phase thermally developing flow experiments coupled with 3-D computational simulations. The major conclusions of the study are as follows:

- Taylor bubbles train flow reduces the average wall temperature and simultaneously increases the fluid temperature which, in turn, enhances the heat transfer as compared to thermally developing laminar single-phase flow. This enhancement in the Nusselt number is about three times that of the fully developed single-phase flow. As compared to thermally developing flow too, the enhancement is between 1.2 to 2.0 times, depending on the axial location where the estimate is compared.
- Increasing volume flow ratio (β), for a fixed liquid mass flow rate results in longer air bubbles, i.e., smaller liquid slugs entrapped between the bubbles. This reduction in the slug length resulted in an increase in the time averaged local Nu, for the present range of experiments.
- It is experimentally and numerically verified that effect of wall axial conduction is minimal for axial conduction number $M < 0.01$. By maintaining a low value of this parameter, the constant heat flux boundary condition can be effectively maintained at the fluid–solid interface.
- With the high resolution temporal measurements of local fluid temperature, the frequency of the bubble train (unit-cell) has been obtained, which compares quantitatively well with slug-flow videography data. Local temporal fluctuations of the wall temperature were not detectable due to the thermal inertia of the wall as compared to the ensuing time scales of the involved thermo-fluid transport process, when an isolated Taylor bubble is injected. This requires future efforts so as to minimize the time response of the wall material.

Increased efforts are needed to design the protocols for measurement of local transport quantities with infra-red thermography, especially at mini/micro scale systems.

Acknowledgements

Financial grants for undertaking this research work, obtained from the Indo-French Center for Promotion of Advanced Research (IFCPAR), are gratefully acknowledged. InfraRed Thermography facility was developed by the grants received from Department of Science and Technology, Government of India.

References

Ajaev, V.S., Homsy, G.M., 2006. Modeling shapes and dynamics of confined bubbles. Ann. Rev. Fluid Mech. 38, 277–307.

Asadolahi, A.N., Gupta, R., Fletcher, D.F., Haynes, B.S., 2011. CFD approaches for the simulation of hydrodynamics and heat transfer in Taylor flow. Chem. Eng. Sci. 66, 5575–5584.
Asadolahi, A.N., Gupta, R., Leung, S.S.Y., Fletcher, D.F., Haynes, B.S., 2012. Validation of a CFD model of Taylor flow hydrodynamics and heat transfer. Chem. Eng. Sci. 69, 541–552.
Astarita, T., Cardone, G., Carlomagno, G.M., Meola, C., 2000. A survey on infrared thermography for convective heat transfer measurements. Opt. Laser Technol. 32, 593–610.
Bajpai, A.K., Khandekar, S., 2012. Thermal transport behavior of a liquid plug moving inside a dry capillary tube. Heat Pipe Sci. Technol. 3, 97–124.
Bao, Z.Y., Fletcher, D.F., Haynes, B.S., 2000. An experimental study of gas liquid flow in a narrow conduit. Int. J. Heat Mass Trans. 43, 2313–2324.
Buchlin, J.M., 2010. Convective heat transfer and infra-red thermography (IRth). J. Appl. Fluid Mech. 3, 55–62.
Bretherton, F.P., 1961. The motion of long bubbles in tubes. J. Fluid Mech. 10, 166–188.
Celata, G.P., Cumo, M., Maconi, V., McPhail, S.J., Zummo, G., 2006. Microtube liquid single phase heat transfer in laminar flow. Int. J. Heat Mass Trans. 49, 3538–3546.
Chen, I.Y., Chen, Y.M., Yang, B.C., Wang, C.C., 2009. Two phase flow pattern and frictional performance across small rectangular channels. Appl. Therm. Eng. 29, 1309–1318.
Cubaud, T., Ho, C.M., 2004. Transport of bubbles in square microchannels. Phys. Fluids 16, 4575–4585.
Dabiri, D., 2009. Digital particle image thermometry/velocimetry: a review. Exp. Fluids 46, 191–241.
Devesenathipathy, S., Santiago, J.G., Werely, S.T., Meinhart, C.D., Takhera, K., 2003. Particle imaging techniques for micro-fabricated fluidic systems. Exp. Fluids 34, 504–514.
Fabre, J., Liñe, A., 1992. Modeling of two-phase slug flow. Ann. Rev. Fluid Mech. 24, 21–46.
Fairbrother, F., Stubbs, A.E., 1935. The bubble tube method of measurement. J. Chem. Soc. 1, 527–529.
Fukagata, K., Kasagi, N., Ua-arayporn, P., Himeno, T., 2007. Numerical simulation of gas–liquid two-phase flow and convective heat transfer in a micro tube. Int. J. Heat Fluid Flow 28, 72–82.
Gupta, R., Fletcher, D.F., Haynes, B.S., 2010. CFD modelling of flow and heat transfer in the Taylor flow regime. Chem. Eng. Sci. 65, 2094–2107.
Han, Y., Shikazono, N., 2009. Measurements of liquid film thickness in micro square channel. Int. J. Multiphase Flow 35, 896–903.
He, Q., Hasegawa, Y., Kasagi, N., 2010. Heat transfer modelling of gas–liquid slug flow without phase change in a micro tube. Int. J. Heat Fluid Flow 31, 126–136.
Hemadri, V.A., Gupta, A., Khandekar, S., 2011. Thermal radiators with embedded pulsating heat pipes: Infra-red thermography and simulations. Appl. Therm. Eng. 31, 1332–1346.
Hetsroni, G., Rozenblit, R., Yarin, L.P., 1996. A hot-foil infrared technique for studying the temperature field of a wall. Meas. Sci. Technol. 7, 1418–1427.
Hetsroni, G., Gurevich, M., Mosyak, A., Rozenblit, R., 2003. Surface temperature measurements of a heated capillary by means of an infrared technique. Meas. Sci. Technol. 14, 807–814.
Hetsroni, G., Mosyak, A., Pogrebnyak, E., Rozenblit, R., 2011. Infrared temperature measurements in micro-channels and micro-fluid systems. Int. J. Therm. Sci. 50, 853–868.
Ide, H., Matsumura, H., 1990. Frictional pressure drops of two phase gas liquid flow in rectangular channels. Exp. Therm. Fluid Sci. 3, 362–372.
Kamisli, F., 2003. Flow of a long bubble in a square capillary. Chem. Eng. Proc. 42, 351–363.
Kashid, M.N., Gerlach, I., Goetz, S., Franzke, J., Acker, J.F., Platte, F., Agar, D.W., Turek, S., 2005. Internal circulation within the liquid slugs of a liquid–liquid slug-flow capillary microreactor. Ind. Eng. Chem. Res. 44, 5003–5010.
Kolb, W.B., Cerro, R.L., 1993. The motion of long bubbles in tubes of square cross sections. Phys. Fluids 5, 1549–1557.
Lee, P.S., Garimella, S.V., Liu, D., 2005. Investigation of heat transfer in rectangular microchannels. Int. J. Heat Mass Trans. 48, 1688–1704.
Lee, P.S., Garimella, S.V., 2006. Thermally developing flow and heat transfer in rectangular microchannels of different aspect ratios. Int. J. Heat Mass Trans. 49, 3060–3067.
Leung, S.S.Y., Gupta, R., Fletcher, D.F., Haynes, B.S., 2012. Gravitational effect on Taylor flow in horizontal microchannels. Chem. Eng. Sci. 69, 553–564.
Majumder, A., Mehta, B., Khandekar, S., 2013. Local Nusselt number enhancement during gas–liquid taylor bubble flow in a square mini-channel: an experimental study. Int. J. Therm. Sci. 66, 8–18.
Maranzana, G., Perry, I., Maillet, D., 2004. Mini- and micro-channels: influence of axial conduction in the walls. Int. J. Heat Mass Trans. 47, 3993–4004.
Mehdizadeh, A., Sherif, S.A., Lear, W.E., 2011. Numerical simulation of thermofluid characteristics of two-phase slug flow in microchannels. Int. J. Heat Mass Trans. 54, 3457–3465.
Mehta, B., Khandekar, S., 2012. Infra-red thermography of laminar heat transfer during early thermal development inside a square mini-channel. Exp. Therm. Fluid Sci. 42, 219–229.
Mishima, K., Hibiki, T., Nishihera, H., 1993. Some characteristics of gas liquid flow in narrow rectangular ducts. Int. J. Multiphase Flow 19, 115–124.
Moharana, M.K., Agarwal, G., Khandekar, S., 2011a. Axial conduction in single-phase simultaneously developing flow in a rectangular mini-channel array. Int. J. Therm. Sci. 50, 1001–1012.
Moharana, M.K., Peela, N.R., Khandekar, S., Kunzru, D., 2011b. Distributed hydrogen production from ethanol in a microfuel processor: issues and challenges. Ren. Sust. Energy Rev. 15, 524–533.
Moharana, M.K., Singh, P.K., Khandekar, S., 2012. Optimum Nusselt number for simultaneously developing internal flow under conjugate conditions in a square microchannel. ASME J. Heat Trans. 134, 071703 (1–10).
Narayanan, C., Lakehal, D., 2008. Two phase convective heat transfer in miniature pipes under normal and micro-gravity conditions. ASME J. Heat Trans. 130, 074502.
Nonino, C., Savino, S., Giudice-Del, S., Mansutti, L., 2009. Conjugate forced convection and the heat conduction in circular microchannels. Int. J. Heat Fluid Flow 30, 823–830.
Rao, M., Khandekar, S., 2009. Simultaneously developing flows under conjugated conditions in a mini-channel array: liquid crystal thermography and computational simulations. Heat Trans. Eng. 30, 751–761.
Sargent, S.R., Hedlund, C.R., Ligrani, P.M., 1998. An infrared thermography imaging system for convective heat transfer measurements in complex flows. Meas. Sci. Technol. 9, 1974–1981.
Serizawa, A., Feng, Z., Kawara, Z., 2002. Two-phase flow in microchannels. Exp. Therm. Fluid Sci. 26, 703–714.
Shah, R.K., London, L.A., 1978. Laminar Flow Forced Convection in Ducts. Academic Press Inc., ISBN: 0120200511.
Spernjak, D., Prasad, A.K., Advani, S.G., 2007. Experimental investigation of liquid water formation and transport in a transparent single-serpentine PEM fuel cell. J. Power Sour. 170, 334–344.
Taha, T., Cui, Z.F., 2004. Hydrodynamics of slug flow inside capillaries. Chem. Eng. Sci. 59, 1181–1190.
Taha, T., Cui, Z.F., 2006. CFD modeling of slug flow inside square capillaries. Chem. Eng. Sci. 61, 665–675.
Talimi, V., Muzychka, Y.S., Kocabiyik, S., 2012a. Numerical simulation of the pressure drop and heat transfer of two phase slug flows in microtubes using moving frame of reference technique. Int. J. Heat Mass Trans. 55, 6463–6472.
Talimi, V., Muzychka, Y.S., Kocabiyik, S., 2012b. A review on numerical studies of slug flow hydrodynamics and heat transfer in microtubes and microchannels. Int. J. Multiphase Flow 39, 88–104.
Taylor, G.I., 1961. Deposition of a viscous fluid on the wall of a tube. J. Fluid Mech. 10, 161–163.
Thulasidas, T.C., Abraham, M.A., Cerro, R.L., 1995. Bubble train flow in capillaries of circular and square cross section. Chem. Eng. Sci. 50, 183–199.
Thulasidas, T.C., Abraham, M.A., Cerro, R.L., 1997. Flow patterns in liquid slugs during bubble train flow inside capillaries. Chem. Eng. Sci. 52 (17), 2947–2962.
Triplett, K.A., Ghiaasiaan, S.M., Khalik, A., Le-Mouel, S.I., McCord, B.N., 1999. Gas-Liquid two-phase flow in microchannels. Part I: Two-phase flow pattern. Int. J. Multiphase Flow 25, 377–394.
Walsh, A.P., Walsh, J.E., Muzychka, S.Y., 2010. Heat transfer model for gas-liquid slug flows under constant flux. Int. J. Heat Mass Trans. 53, 3193–3201.
Zaloha, P., Kristal, J., Jiricny, V., Volkel, N., Xuereb, C., Aubin, J., 2012. Characteristics of liquid slugs in gas–liquid Taylor flow in microchannels. Chem. Eng. Sci. 68, 640–649.